

Interplay of Structure and Dynamics in Solid Polymer Electrolytes: a Molecular Dynamics Study of LiPF₆/polypropylene carbonate

Amaury Coste,^{*,†} Thomas Meyer,[‡] Claire Villevielle,[‡] Fannie Alloin,[‡] Stefano Mossa,[†] and Benoit Coasne^{*,¶,§}

[†]*Univ. Grenoble-Alpes, CEA, IRIG-MEM-L Sim, 38000 Grenoble, France*

[‡]*Univ. Grenoble Alpes, Univ. Savoie Mont Blanc, CNRS, Grenoble INP, LEPMI, 38000 Grenoble, France*

[¶]*Université Grenoble Alpes, CNRS, LIPhy, Grenoble, 38000, France*

[§]*Institut Laue Langevin, 38042 Grenoble, France*

E-mail: amaury.coste@cea.fr; benoit.coasne@univ-grenoble-alpes.fr

Abstract

Solid-state batteries (SSB) are emerging as the next generation of electrochemical energy storage devices. In this context, obtaining high energy density batteries relies on the use of solid polymer electrolytes (SPE) that are electrochemically stable with respect to lithium metal and high potential positive electrode (both conditions being difficult to achieve without chemical degradation). Here, molecular dynamics simulations are used to investigate the interplay of structure and dynamics of carbonate-based SPE made up of polypropylene carbonate and lithium hexafluorophosphate (LiPF₆) at salt concentrations ranging from 0.32 to 1.21 mol/kg. On the one hand, the structural properties of such SPE are studied under ambient pressure and at the experimentally

relevant temperature $T = 353$ K. On the other hand, considering that the very slow processes involved in these systems are out-of-reach of molecular dynamics, the dynamic properties are simulated at high temperature up to 900 K and then extrapolated to $T = 353$ K using Arrhenius' law. Our results reveal strong ionic correlations with a limited fraction of free ions and a prevalence of negatively charged clusters (particularly at the highest salt concentrations). The self-diffusion coefficient of Li^+ exceeds that of PF_6^- at high temperature due to the weaker Li^+ -carbonate and ion-ion interactions. However, the Li^+ mobility at $T = 353$ K is lower than that of the anion, in agreement with the typical experimental SPE behavior reported in the literature. As expected, our MD simulations show that the ionic conductivity σ increases with temperature. Moreover, σ at $T = 353$ K exhibits a maximum at a salt concentration between 1.0 and 1.1 mol/kg. Overall, our estimated physico-chemical parameters indicate that strong ion correlations can be optimized to design better SPE. In this context, the Arrhenius extrapolation approach employed here provides insights into ion transport mechanisms in SPE.

1. Introduction

With the increasing demand for high-energy-density devices, solid-state batteries (SSB) are considered promising for electrochemical energy storage.¹⁻³ Compared to conventional lithium-ion batteries that rely on a liquid electrolyte, SSB provide (1) higher energy density through the use of lithium metal as negative electrode and (2) enhanced safety by suppressing flammable organic solvent.⁴⁻⁶ In practice, solid electrolytes are classified in two main categories: solid polymer electrolytes (SPE) and ceramic electrolytes (CE). Due to their brittle nature, CE are difficult to manufacture – especially considering that they need to be densified to be used (therefore causing issue for electrode preparation where intimate contact must be achieved between the active material, the conductive additive, and the solid electrolyte). In contrast, SPE are cheap and flexible materials which are easy to manufacture

and can be mixed easily with other electrode components.⁷⁻⁹ As a result, features of the polymer material in SPE [e.g. poly(ethylene oxide) polymer (PEO)] have been investigated since the 1970's and PEO-based SPE have been commercialized.¹⁰⁻¹⁴

However, SPE exhibits low ionic conductivities at room temperature due to PEO crystallinity and slow dynamics with this high molecular weight polymer.¹⁵ In addition, due to the weak stability of the ether function against oxidation (which occurs at 3.7 V *vs.* Li⁺/Li), it is not possible to use high voltage electrode materials such as those of the NMC family [Li_xNi_aMn_bCo_cO₂, with (a+b+c=1)]. In fact, only a limited number of coordinating polymers display good electrochemical stability at high voltage. Chemically, these polymer electrolytes should contain polar groups such as carbonate or nitrile functions.¹⁶ In this context, polypropylene carbonate polymers (PPC) have proven to be a valid alternative to PEO.¹⁷⁻²³ In fact, it is a low-cost and biodegradable polymer²⁴ with a chemical structure which closely resembles that of conventional carbonate-based electrolytes (therefore implying good compatibility with lithium salts and favorable interfacial contact with conventional electrodes).^{25,26} Unfortunately, these polymers have high glass transition temperatures T_g leading to slow ionic/polymer mobility and conductivity at room temperature.⁹

Optimizing the electrochemical performance of SPE-based batteries requires enhancing the transport of ionic species which, in turn, necessitates a detailed understanding of the system's structural and dynamic properties.^{27,28} While extensive studies using all-atom^{29,30} and coarse-grained³¹⁻³³ Molecular Dynamics simulations have focused on the structural and dynamic properties of PEO/LiTFSI-based SPEs, PC-based SPEs have received significantly less attention.³⁴ To address this knowledge gap, we use here molecular modeling to investigate the interplay between the structure and dynamics of LiPF₆/PPC-based SPE as a function of the salt concentration c_s . In more detail, to provide a comprehensive picture of the underlying molecular mechanisms at play, we simulate SPE at different salt concentrations c_s from 0.32 to 1.21 mol/kg (which correspond to carbonate/salt ratios $R_{C/Li}$ varying from 30 to 8). To shed light on the interplay between structural and dynamical properties in

LiPF_6/PPC -based SPE, we investigate the properties of the polymer matrix, ionic local coordination shell, and the dissociation state of the salt in the electrolyte (free ions, ion pairs, ion clusters) as a function of the salt concentration c_s . The dynamic and transport properties – including the ion diffusion coefficient D_s and conductivity σ – are determined at several high temperatures T . Arrhenius' law is then employed to extrapolate the behavior at low temperatures relevant to the practical use of SPE. Based on these data, we provide an atom-scale description of the structure and dynamics of PPC-based SPE as a function of the salt concentration/temperature, which can contribute to the design of high-performance solid electrolytes.

2. Experimental and Computational Methods

2.1. Experimental Section

To validate the relevance of the atomistic model employed in MD, we measured the density of several PPC-based SPEs at different salt concentrations c_s . In what follows, we provide details on the polymer electrolyte elaboration and the density measurements performed.

Polymer electrolyte elaboration. The polymer electrolytes were prepared in an argon-filled glovebox (H_2O and O_2 concentration < 0.1 ppm). Polypropylene carbonate – hereafter called PPC, ($\text{Mn} = 50,000$ by GPC, Sigma-Aldrich, stored at -20°C) – was used as received while lithium hexafluorophosphate LiPF_6 (Tokyo Chemical Industry, purity $> 97.0\%$, stored under Ar) was used after drying for 2 days under dynamic vacuum at 110°C . Three polymer electrolytes with various lithium contents were prepared together with a reference material composed of pure PPC. The polymer and the lithium salt were dissolved in acetonitrile (Sigma-Aldrich, anhydrous, purity 99.8%). After 2 hours of magnetic stirring at 200 rpm at a temperature of 80°C , homogeneous solutions were cast in Petri dishes. The samples were then dried overnight at 60°C under dynamic vacuum.

Density Measurements. To estimate the density of each sample, a Mettler Toledo 33360 density determination kit was used. The kit is based on the Archimedes principle, which is particularly useful for irregularly shaped solids such as polymers. Here, we employed heptane (Sigma-Aldrich, purity $\geq 99.99\%$) that does not dissolve or swell the polymer electrolyte. The experiments were carried out at room temperature in an argon-filled glovebox (H_2O and $\text{O}_2 < 0.1$ ppm).

2.2. Molecular Simulation Section

SPE molecular model. Fig. 1 shows a typical molecular configuration of our LiPF_6/PPC model together with a zoomed view of the different chemical species that form this SPE. Each simulation box contains PPC chains made up of 40 monomers, therefore leading to a molecular weight of 4,100 g/mol. Although this value is about 120 times smaller than that of the average experimental polymer chain, we believe our polymer chains are sufficiently long to behave like the experimental system on time scales considered in MD. In practice, the polymer lengths considered here are similar to those employed in other MD simulations on PPC-based SPE.³⁴ The ends of the chains were symmetrised and terminated with isopropyl groups $\text{CH}(\text{CH}_3)_2$. The electrolyte compositions considered in the present work are reported in Table 1. In practice, we modeled five SPEs together with the pure polymer. Note that the number of PPC chains (and, therefore, the total number of carbonate groups) remains constant in all cases, while the number of ion pairs varies to match the target salt concentration c_s . In addition, to analyze the role of the electrostatic interactions and of the polymer matrix on ion mobility, we simulated both the pure polymer melt and the electrolyte mixture with $R_{\text{C/Li}} = 8$ for a system formed by substantially shorter chains (comprising only three monomers). In any case, the total number of carbonate groups is about the same as that for the long chain case so that the comparison between short and long chains is made for the same ionic concentration c_s .

Table 1: Composition of the LiPF_6/PPC SPE considered in Molecular Dynamics. For every salt concentration c_s , the carbonate/salt $R_{\text{C/Li}}$, the number of LiPF_6 ions N_{salt} and the number polymer chains $N_{\text{pol.}}$ for the long (40 monomers) and short (3 monomers) chains are reported.

	c_s (mol/kg)	$R_{\text{C/Li}}$	N_{salt}	$N_{\text{pol.}}$
long chain	-	-	-	40
	0.32	30	53	40
	0.48	20	80	40
	0.61	16	100	40
	0.81	12	133	40
	1.21	8	200	40
short chain	-	-	-	533
	1.21	8	200	533

Bonded and non-bonded interactions for the polymer were described using the OPLS-AA force field³⁵ with partial atomic charges taken from Ref.³⁶ The Li^+ and PF_6^- ions were described using the CL&P force field.^{37,38} With this force field, geometric mixing rules are applied to determine the Lennard-Jones parameters for the polymer/polymer interactions, whereas arithmetic mixing rules are employed for all other cross-interactions. The partial charges of the ions were scaled by a factor of 0.8 to account in an effective fashion for polarization effects and improve the description of ion dynamics as demonstrated in previous works.^{34,39,40} All molecular simulations were performed with periodic boundary conditions applied in the x , y , and z directions. Non-bonded interactions were calculated within a cutoff distance $r_c = 12 \text{ \AA}$. Long-range electrostatic interactions were evaluated with the PPPM solver.⁴¹ All simulations were carried out with LAMMPS.⁴²⁻⁴⁴ Newton's equation of motion was integrated using the velocity-Verlet algorithm^{45,46} with a time step $\delta t = 1 \text{ fs}$. At $T = 900 \text{ K}$, we used a shorter time step $\delta t = 0.5 \text{ fs}$. Note that in all cases the C-H bonds were constrained using the SHAKE algorithm.⁴⁷ We employed the Nosé-Hoover thermostat⁴⁸ with a coupling constant $\tau_T = 0.1 \text{ ps}$. For the NPT simulations at $P = 1.0 \text{ bar}$, we additionally coupled the systems to a Nosé-Hoover barostat with a relaxation time $\tau_P = 1.0 \text{ ps}$.

Preparation protocol. In order to prepare initial configurations for the SPE listed in

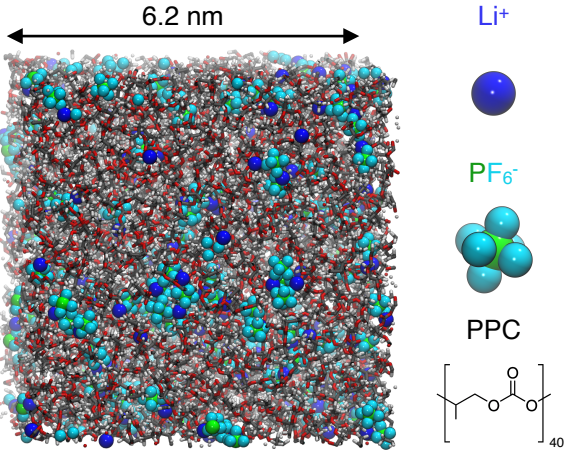


Figure 1: Typical molecular configuration of the molecular model of LiPF₆/PPC SPE. The Li⁺ cations are shown as blue spheres while the PF₆⁻ anions are shown as green and cyan spheres. The PPC chains are made up of 40 monomers where the carbon, oxygen and hydrogen atoms are shown as gray, red and white spheres, respectively. The monomer chemical composition and structure are shown in the bottom right of the figure.

Table 1, we employed the same thermodynamic path in a systematic fashion. In brief, we prepared the initial configuration using a 200 ps NVT run at constant volume and a temperature of $T = 1500$ K with a box length $L = 60$ nm. At this very low density, the system consists of an ideal gas of polymer chains and ions (in this initial phase, the charge of the salt ions were set to zero to avoid ion pairing/precipitation). Then, starting from this initial configuration, we performed an NPT run at $T = 1500$ K and $P = 1$ bar for 1 ns to condense the system and reach the volume corresponding to ambient pressure. This condensation step was followed by a 500 ps annealing from $T = 1500$ K to 1000 K at constant volume V . The system was then further condensed at $T = 1000$ K at constant atmospheric pressure for 1 ns to eventually reach a density of about 0.9-1.0 g/cm³ (followed by an additional 1 ns annealing from $T = 1000$ K to 700 K at constant volume and a longer relaxation at constant volume over 5 ns at the latter temperature). Finally, we further reduce the temperature from 700 to 353 K during 5 ns at constant ambient pressure $P = 1$ bar. At this point, the ion partial charges were set to their actual values and the system was

equilibrated at $T = 353$ K and $P = 1$ bar for 40 to 50 ns to reach the final constant density.

We note that the relaxation time of the PPC-based SPE at $T = 353$ K is much longer than the timescales accessible with molecular dynamics simulations since the system's viscosity is typically of the order of a few MPa·s.⁴⁹ As a consequence, the dynamics that we can reasonably probe/access at room temperature mostly consists of localised rearrangements of the polymer matrix. To reasonably quantify the transport properties at each salt concentration, we therefore performed molecular simulations at higher temperatures: $T = 600, 650, 700, 800$, and 900 K. In practice, we started from $T = 353$ K and applied sequential temperature ramps of 15 ns each to reach the target temperature. Each ramp was conducted at constant volume, therefore resulting in a temperature increase along isochores corresponding to the density of the ambient system at $T = 353$ K for each concentration. At every temperature, we eventually performed a long equilibration in the NVT ensemble for 50 ns followed by the production run sufficiently extended to reach the diffusive (i.e., Fickian) regime for all systems.

3. Results

3.1. Structural properties

Polymer nanostructure. We determined the structural properties of the system at $T = 353$ K and at ambient pressure using MD trajectories of 60 ns. Fig. 2(a) shows both the total electrolyte mass density ρ and that of the polymer matrix ρ_p as a function of the salt concentration c_s . A linear increase in the SPE density is observed upon increasing c_s , which is mirrored by an opposite trend for ρ_p . This result indicates that the addition of salt increases the volume occupied by the polymer while increasing the overall density of the system because of the added salt ions. The accuracy of our modeling can be assessed by comparing the computed total density with the experimental results obtained as detailed in the experimental methods section. Fig. 2(b) shows both data sets for the pure polymer and

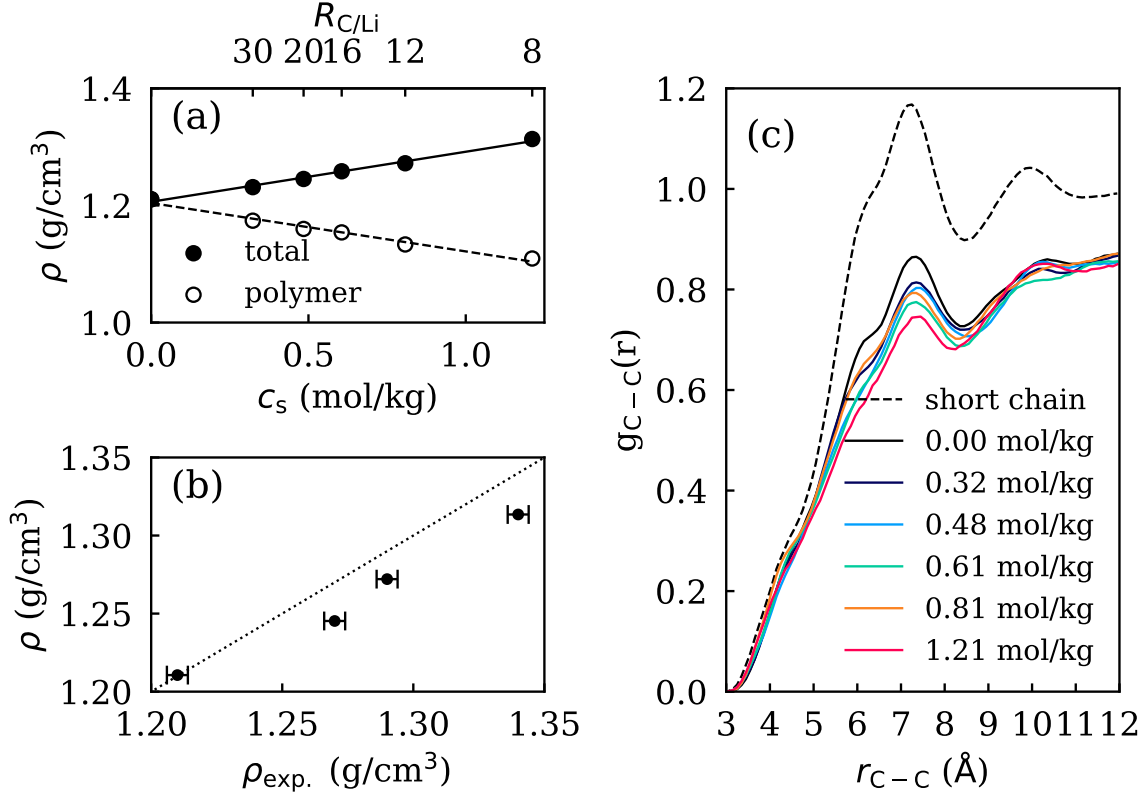


Figure 2: (a) Computed total density ρ and polymer matrix density ρ_p (without considering the salt mass) as a function of the salt concentration c_s . (b) Computed *versus* experimental densities ρ for the different SPEs considered in this study. The dashed line indicates the condition $\rho = \rho_{\text{exp}}$. (c) Intermolecular radial distribution function $g_{\text{C-C}}(r)$ between the C atoms of the carbonate function for the short chain polymer $n = 3$ without salt (black dashed line), the long chain polymer $n = 40$ without salt (black solid line) and SPEs with different salt concentrations (solid color lines).

SPE with three different concentrations [$c_s = 0.48$, 0.81 , and 1.21 mol/kg]. Although our simulations slightly underestimate the experimental density at all concentrations, the linear trend observed experimentally is reproduced quite satisfactorily using molecular dynamics.

We also assessed the details of the polymer nanostructure by computing the partial radial distribution functions defined as

$$g_{\alpha\beta}(r) = \frac{V}{N_\alpha N_\beta} \sum_{i=1}^{N_\alpha} \sum_{j=1}^{N_\beta} \langle \delta(r - |\vec{r}_j - \vec{r}_i|) \rangle, \quad (1)$$

where N_α and N_β are the numbers of atoms of type α and β while \vec{r}_i and \vec{r}_j are the positions of

atoms i and j . Fig 2(c) shows $g_{CC}(r)$ for the carbon atom of the carbonate group at different concentrations c_s (intramolecular interactions between carbon atoms of the same chain were excluded). We also report the polymer structure for the short-chain polymer ($n = 3$) without salt and for the long-chain polymer ($n = 40$) without salt. The radial distribution function $g_{CC}(r)$ for short polymer chains without salt (black dashed line) exhibits a well-defined main peak at 7 Å followed by a minimum at 8.5 Å and a second peak at 10 Å (such nanometric structure is similar to what is typically observed for liquid solvents). For the long-chain polymer without salt, the radial distribution function $g_{CC}(r)$ (solid black line) displays peaks at the same positions, although their amplitude decreases due to polymer entanglement.

Despite small variations in the peak amplitudes, the radial distribution function $g_{CC}(r)$ does not show any shift in the peak positions upon changing the concentration c_s . This finding can be attributed to the small size of the salt ions and the low to moderate salt concentrations considered in the present study. Note that we prepared the systems at each concentration independently of each other to minimize correlations among the different numerical samples. The absence of marked impact of the concentration c_s on the polymer nanostructure was confirmed by calculating in Table 2 the gyration radius R_g , the head-to-tail distance l_{h-t} , and the interchain carbon-carbon contact number $N_{inter-chain}$ as a function of c_s . On average, $R_g \sim 12$ Å and $l_{h-t} \sim 35$ Å show no pronounced dependence on c_s . On the other hand, $N_{inter-chain}$ decreases slightly but in a monotonous fashion with c_s due to the insertion of more and more ions between the polymer chains. Altogether, these results show that the addition of salt – at least in the range of concentrations explored in this study – does not induce significant modifications of the polymer structure.

Ion coordination. The structural features of the ions (Li^+ and PF_6^-) were also analyzed using partial radial distribution functions calculated at $T = 353$ K. The $g_{\alpha\beta}(r)$ functions (left y -axis) together with the associated coordination numbers $CN_{\alpha\beta}(r)$ (right y -axis) are shown in Fig. 3 for $\alpha = \text{Li}/\beta = \text{O}$, $\alpha = \text{P}_{\text{PF}_6^-}/\beta = \text{O}$, and $\alpha = \text{Li}/\beta = \text{P}_{\text{PF}_6^-}$ for different salt concentrations c_s . For the cation-carbonate correlations in Fig. 3(a), we observe two peaks

Table 2: Average and standard deviation (in parentheses) of the polymer gyration radius R_g , head to tail distance l_{h-t} , and interchain contact number $N_{inter-chain}$ for the SPE at $T = 353.15$ K and different concentrations c_s .

c_s (mol/kg)	$R_{C/Li}$	R_g (Å)	l_{h-t} (Å)	$N_{inter-chain}$
0.00	-	12.0 (3.0)	34.3 (13.2)	3.1 (0.22)
0.32	30	11.4 (2.5)	32.4 (13.7)	2.9 (0.25)
0.48	20	11.8 (2.7)	33.4 (11.6)	2.8 (0.22)
0.61	16	11.9 (4.0)	34.6 (16.6)	2.7 (0.23)
0.81	12	12.2 (3.0)	37.5 (11.6)	2.7 (0.23)
1.21	8	11.9 (3.0)	36.1 (10.8)	2.6 (0.25)

at distances of 1.93 Å and 4.02 Å, respectively. The first peak, which corresponds to the formation of a closed packed coordination shell extending to $\simeq 3$ Å, is in good agreement with previous *ab initio* molecular dynamics results for LiTFSI/Propylene carbonate liquid electrolytes.⁵⁰ Correspondingly, the coordination number at 3 Å decreases from 3.8 to 2.9 as the salt concentration c_s increases from 0.32 to 1.21 mol/kg. This decrease is correlated with the increase in the number of ions in the solution, which leads to the formation of contact ion pairs and ion clusters as will be discussed below. The second peak at $\simeq 4.02$ Å arises from the interaction with oxygen atoms which belong to the interacting carbonate groups but are not directly in contact with the Li^+ cation. Again, the position of the peaks are not modified upon varying c_s . The anion/carbonate correlations probed in Fig. 3(b) become non-negligible at distances larger than the radius of the cation/carbonate coordination shell with moderate peaks at 4.3 Å and 6.0 Å, respectively. It has to be noticed that the amplitudes are close to 1. At all salt concentrations c_s , the corresponding coordination number is negligible for distances smaller than 4.3 Å and then increases steeply up to $\simeq 6$ at the first minimum observed at 5.0 Å. No modifications of the peak positions are observed with c_s , while the amplitude slightly increases with the concentration c_s .

Cation/anion structural correlations are shown in Fig. 3(c). Two partially overlapping peaks are observed at about 2.3 Å and 3.44 Å together with an additional weaker peak at around 7.4 Å. These peaks correspond to two coordination modes: bidentate Li^+ (first peak)

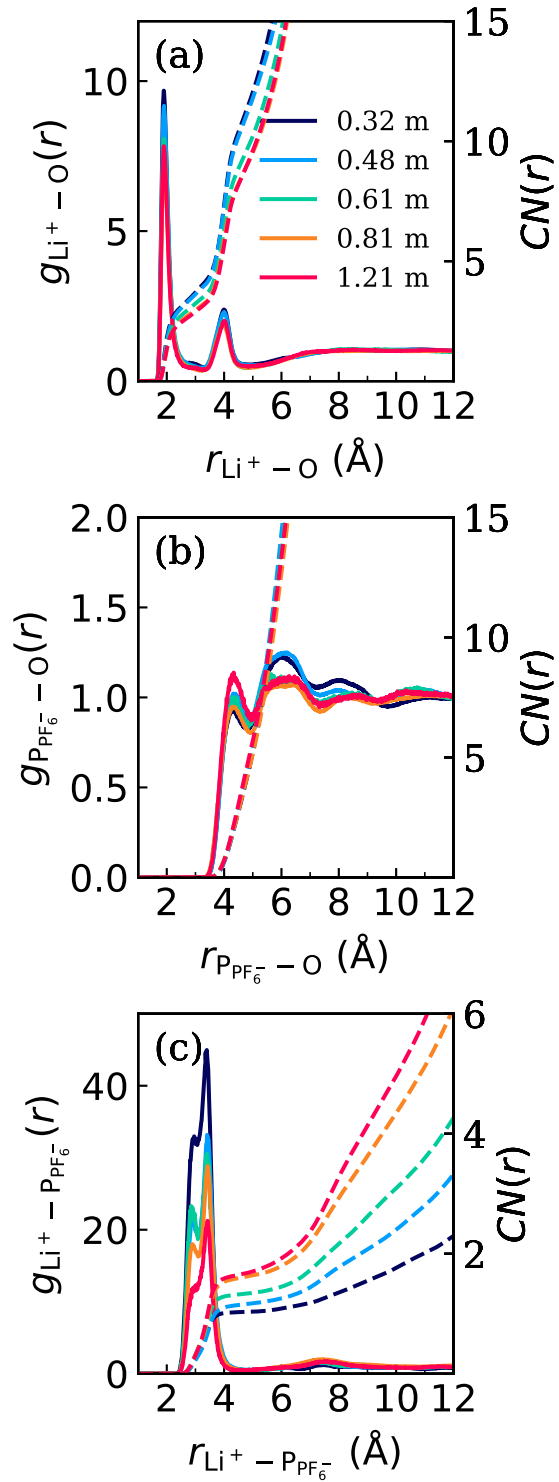


Figure 3: Partial radial distribution function $g(r)$ (solid lines) and associated coordination number $CN(r)$ (dashed lines) at $T = 353$ K: (a) $\text{Li}^+ \text{-} \text{O}$, (b) $\text{P}_{\text{PF}_6}^- \text{-} \text{O}$ and (c) $\text{Li}^+ \text{-} \text{P}_{\text{PF}_6}^-$.

and monodentate Li^+ (second peak). The peak positions are in agreement with previous density functional theory (DFT) calculations⁵¹ for $\text{Li}^+ \text{-} \text{PF}_6^-$ interactions in a poly(ethylene oxide) matrix. The peak at 7.4 Å corresponds to correlations of co-ions belonging to the same ionic cluster, which will be analysed in detail in the following. We also note that the coordination number $CN(r)$ in the first coordination shell increases from 1.0 to 1.7 as the salt concentration c_s increases. A value larger than unity confirms that ions form both contact ion pairs and ionic clusters $[\text{Li}_x(\text{PF}_6)_y]^{x-y}$. As expected, such ion pairs and clusters are more frequent at high salt concentrations, as will be discussed in detail below.

A comprehensive view of the local coordination of Li^+ can be obtained by counting the number of oxygen (carbonate units) and fluorine (PF_6^- anion) atoms comprised in spheres centered on Li^+ and with a radius $\simeq 3.1$ Å (corresponding to the position of the first minimum in the associated radial distribution functions, see Fig. 3(a) and S1). Fig. 4(a) shows the salt concentration dependence of the total (black) coordination number together with the associated number of oxygen (red) and fluorine (blue) atoms contained in the sphere. The total CN remains almost constant at about $\simeq 5$ upon increasing c_s . However, the situation is different for the partial contributions as CN for fluorine atoms increases while CN for oxygen atoms decreases. This suggests that the anions gradually replace the oxygen atoms in the coordination shell of the cation upon increasing the salt concentration c_s . This finding has already been observed in other systems such as the Li^+ cation with different carbonate solvents – typically at salt concentrations close to 1 mol/L. For ethylene carbonate, four oxygen atoms have been found in the first solvation shell using both classical MD^{52,53} and DFT calculations.^{54,55} Similarly, in propylene carbonate-based electrolytes, a value of 4.5 oxygen atoms have been reported in the first solvation shell of Li^+ cation using time-of-flight neutron experiments.⁵⁶ In contrast, for dimethyl carbonate DMC, the first coordination shell of the Li^+ consists on average of 2.8 solvent molecules and 1.1 PF_6^- anions.⁵⁷

Our molecular simulation data also provide quantitative information about the extended ionic domains that form at high salt concentrations c_s . To describe and quantify the asso-

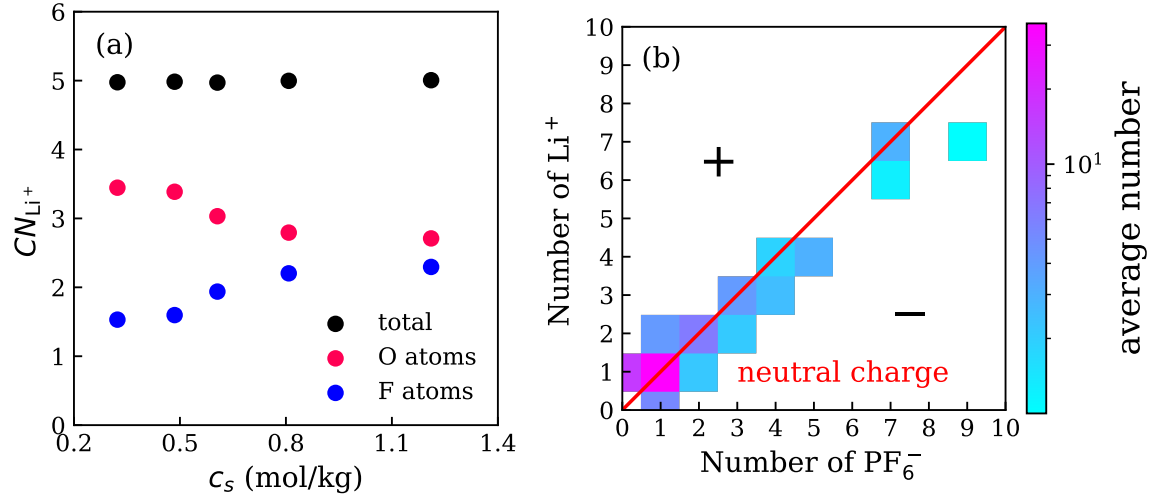


Figure 4: (a) Coordination number of the first coordination shell of the Li^+ cations CN_{Li^+} as a function of c_s . The total CN_{Li^+} and individual contributions with O and F atoms are shown in black, red and blue, respectively. The coordination shell is defined with a cutoff radius of 3.1 Å based on the data shown in Figure 2.(a) and Fig. S1 of the Supporting Information. (b) Distribution of ion cluster $[\text{Li}_x(\text{PF}_6)_y]^{x-y}$ for the SPE at $c_s = 1.21 \text{ mol/kg}$. Li^+ and PF_6^- ions are considered to belong to the same cluster if they formed a contact ion pair CIP ($r_{\text{Li}-\text{P}} \leq 5.1 \text{ \AA}$). The red line represents equimolar (i.e., neutral) clusters where the number of cations and anions are equal.

ciation/dissociation states of the salt in SPE, we have used a graph approach to evaluate the global ionic connectivity network.⁵⁸ In practice, we associate (1) network nodes to the centers of mass of all ions and (2) network edges based on the distance criterium $\text{Li}^+ - \text{P}_{\text{PF}_6^-} \leq 5.1 \text{ \AA}$ (the latter corresponds to the boundary of the coordination shell as described above). This procedure allows us to determine the speciation of the ions in the SPE and to identify three different states for both ions: *i*) free (bare) ions (i.e. without any counterions in the first coordination shell); *ii*) contact ion pairs $\text{Li}^+ \text{PF}_6^-$ (CIP); and *iii*) ion clusters made up of three or more ions. Fig. 4(b) shows a color map of the number of ion clusters with a given cation/anion composition occurring in each SPE (these data are averaged over the entire MD trajectory). Here, we consider the SPE with the largest salt concentration $c_s = 1.21 \text{ mol/kg}$. The red solid line corresponds to the condition of neutral clusters (equal number of cations/anions) so that it delimits positively charged clusters (above the line)

Table 3: Average distribution of Li^+ cations and PF_6^- anions in three different states: free ions, LiPF_6 contact ion pairs (CIP), and ion clusters $[\text{Li}_x(\text{PF}_6)_y]^{x-y}$. Free single ions are defined as ions with no counterion within the first cation/anion coordination shell. The other ions form either CIP or ion clusters.

c_s (mol/kg)	Free single ions (%)		ions in CIP (%)		ions in cluster (%)	
	Li^+	PF_6^-	Li^+	PF_6^-	Li^+	PF_6^-
0.32	24	15	43	43	33	42
0.48	15	6	43	43	42	51
0.61	16	5	31	31	53	64
0.81	13	3	23	23	64	74
1.21	8	3	18	18	74	79

and negatively charged clusters (below the line). For the sake of clarity, considering that the simulation box contains 200 cations and 200 anions at this concentration, we only considered in this plot clusters and CIP with an occurrence of at least 1 per molecular configuration. These data show that CIP is the most common ionic form followed by free Li^+ and then small clusters of size (≤ 4). While the later can be positively charged, negatively charged, or neutral, large clusters tend to be neutral or negatively charged. It has to be noticed that the number of clusters is statistically small. However, the trend is consistent with previous observation obtained by means of classical molecular dynamics for LiTFSI/PEO-based SPE.⁵⁹ Table 3 shows the percentage of the three co-ion states for different c_s . The same data obtained at higher temperatures are shown in Table S1 of the Supporting Information. Only small fractions of free ions are observed for the SPE at the highest concentration c_s . The fraction of free cations is about three times larger than that of free anions, therefore resulting in the formation of negatively charged clusters. The number of CIP is also significant as it represents almost 20 % of the total salt content. As expected, upon lowering c_s , the fractions of CIP and free ions increase whereas the fraction of ion clusters decreases. Also, we note that the overall speciation distribution does not show any substantial modification at higher temperatures as can be seen in Table S1 of the Supporting Information.

The large ionic association in SPE can be explained by estimating the dielectric constant

ϵ of the polymer matrix from the dipole moment fluctuations,⁶⁰

$$\epsilon/\epsilon_0 = \frac{1}{3Vk_B T}(\langle M^2 \rangle - \langle M \rangle^2). \quad (2)$$

We obtain $\epsilon = 1.3 \epsilon_0$, which is quite small and of the order of magnitude of the experimental value $\epsilon = 3.0 \epsilon_0$ at room temperature.^{61,62} This result contrasts with the case of cyclic carbonates, which exhibit a high dielectric constant – $\epsilon \simeq 65$ and $\epsilon \simeq 95$ for propylene and ethylene carbonate, respectively.^{63–65} For the linear carbonate solvents and polymer carbonates (such as that considered here), the organization and solvation properties are different and the electrostatic screening of the charge is weaker – therefore limiting salt dissociation. Also, the dielectric constant was studied by classical MD for liquid electrolytes at different temperatures and electrolyte compositions (of particular relevance to the present work, the system DMC/LiPF₆ was studied⁶⁶). The results revealed similar *CN* to those observed for our SPE. Furthermore, the DMC solvent exhibits a low dielectric constant ($\epsilon_{\text{MD}} \simeq 1.44\epsilon_0$ and $\epsilon_{\text{exp}} \simeq 3.17\epsilon_0$).

3.2. Dynamics and transport

Ionic Diffusion. We calculated the self-diffusion coefficients D_s for the cations and anions at temperatures ranging from $T = 700$ K to 900 K. In more detail, using the Einstein relation, we extracted D_s from the ionic mean squared displacements $\langle \Delta r^2(t) \rangle$ (Fig. S3) in the long time limit (e.g. Fickian regime):^{67,68}

$$D_s = \frac{1}{6} \lim_{t \rightarrow \infty} \frac{d \langle \Delta r^2(t) \rangle}{dt}, \quad (3)$$

Fig. 5(a) shows D_s for the Li⁺ cations (circle) and the PF₆⁻ anions (open circle) as a function of c_s at $T = 700$ K, 800 K and 900 K. As expected, increasing the temperature increases the diffusion of ions at all concentrations c_s . For Li⁺, D_s is almost concentration independent in the range from $T = 700$ K to $T = 800$ K while it decreases as c_s increases at $T = 900$ K. In

contrast, for PF_6^- , D_s decreases upon increasing c_s at all temperatures T .

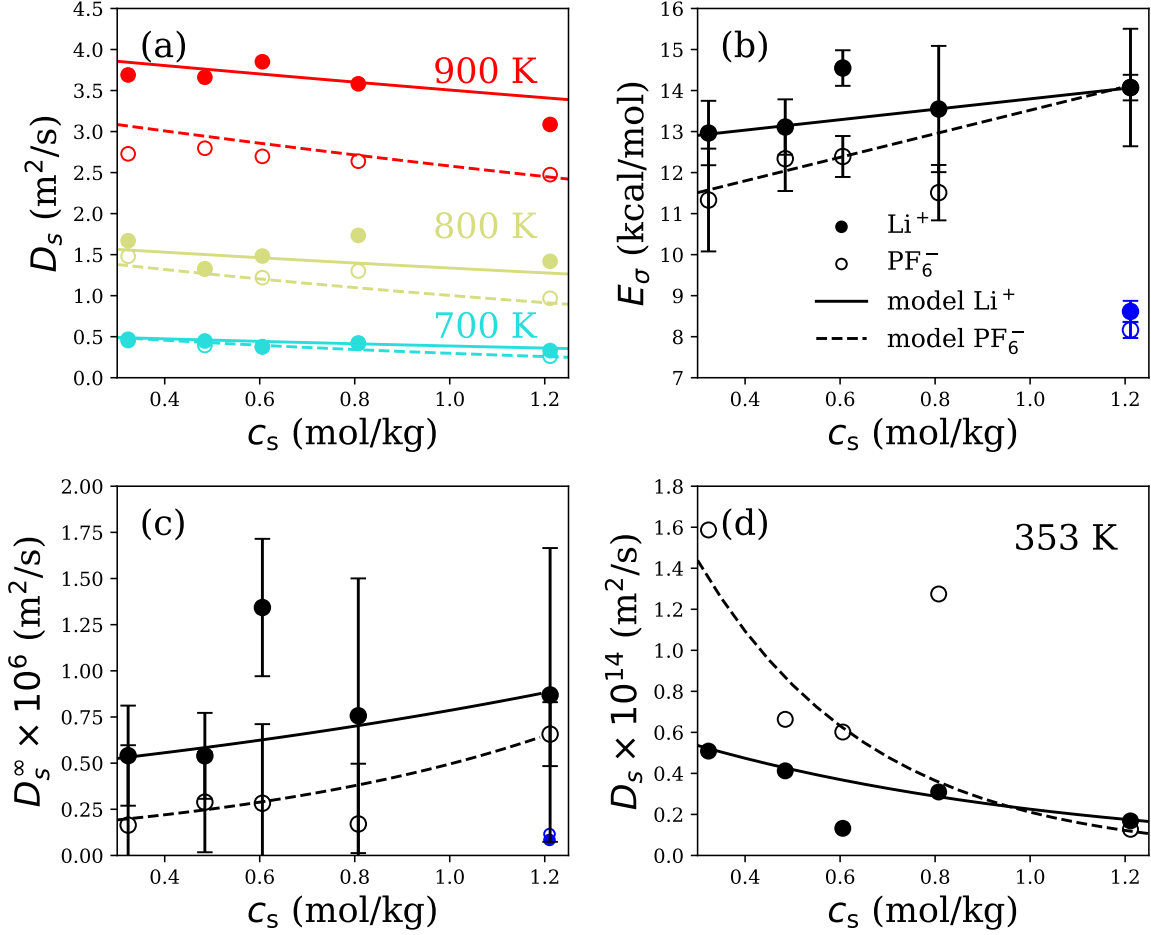


Figure 5: (a) Self-diffusion coefficients D_s of Li^+ cation (closed circle) and PF_6^- anion (open circle) as a function of c_s . The data are shown at $T = 700 \text{ K}$ (cyan), $T = 800 \text{ K}$ (orange) and $T = 900 \text{ K}$ (red). (b) Activation energy E_a for diffusion and (c) D_s^∞ calculated at every salt concentration c_s for the cations Li^+ (close circle) and the anions PF_6^- (open circle). The dark blue data represent the values obtained when using SPE short chains. The line corresponds to the models employed for E_a and D_s^∞ which are the parameters in Arrhenius' law. (d) The lines show the extrapolated self-diffusion coefficients at $T = 353 \text{ K}$ as inferred from Arrhenius' law for Li^+ cations (closed circle) and PF_6^- anions (open circle).

We can extrapolate these data using an Arrhenius law to predict the cation and anion diffusion coefficients at the experimental temperature $T = 353 \text{ K}$. As already explained, this approach allows us overcoming the fact that the relaxation time scale near room temperature exceeds those that can be reached using molecular dynamics. In practice, for each concen-

tration c_s , we have fitted our data at high temperatures against Arrhenius' law (Fig. S4):

$$D_s(c_s, T) = D_s^\infty(c_s) \exp\left(-\frac{E_a(c_s)}{RT}\right), \quad (4)$$

where D_s^∞ is the diffusivity at infinite temperature – that is where the thermal energy largely exceeds the activation energy for diffusion E_a . Here, we note that the Vogel-Tamman-Fulcher (VTF) equation is often used to fit the transport properties of SPE because it takes into account the correlation between the ion transport and the segmental motion of the polymer.^{69,70} However, considering that our molecular simulations were conducted at temperatures significantly above the glass transition temperature, we found that Arrhenius' law accurately describes the physics at play for both ions as shown in Figs. S4 and S5 of the Supporting Information.

Fig. 5(b) shows the concentration dependence of E_a for the cation Li^+ (red) and the anion PF_6^- (black). For the Li^+ cation, E_a increases rather linearly with c_s as illustrated by the black line. However, we note that the overall increase in E_a is quite small as E_a remains very close to the average value of $\simeq 13.5$ kcal/mol. In fact, taking E_a as a constant would not modify the conclusions drawn below. For the PF_6^- anion, E_a increases linearly with a more pronounced variation with c_s from 11.3 kcal/mol at low salt concentration to 14.1 kcal/mol at high salt concentration. At the concentration $c_s = 1.21$ mol/kg, E_a is almost equal for both ions due to the low dissociation state for this concentration. In addition, we also show in the same figure our results for the SPE at 1.21 mol/kg when the long polymer chains are replaced by short chains. In that case, E_a is significantly lower with a value of about $\simeq 9$ kcal/mol for both ions. The variation of E_a is mainly due to the polymer mobility since the dissociation state and the dielectric constant for both systems are similar. Indeed, the fast dynamics of the short polymer chains necessarily decreases the activation energy and, hence, promotes ion diffusion and transport. Fig. 5(c) shows the prefactor D_s^∞ for the cation Li^+ (in red) and the anion PF_6^- (in black). In both cases, D_s^∞ increases with the salt

concentration c_s . Like for E_a , as a first-order approximation, we can fit $\ln D_s^\infty(c_s)$ against an exponential function with a linear argument.

With our fits for $E_a(c_s)$ and $D_s^\infty(c_s)$, we can now predict the diffusivities of the ions at any concentration c_s and temperature T using Eq. (4). The results of this interpolation/extrapolation (solid and dashed lines) are found to be in reasonable agreement with our molecular simulation data (symbols) in Fig. 5(a). Using this procedure, we can extrapolate the values of $D_s(c_s, T)$ to experimentally relevant temperature conditions as shown in Fig. 5(d). A few observations are in order here. First, while Li^+ cation diffusion is faster than that of the PF_6^- anion at high temperatures, an inversion in the self-diffusivity of the anion/cation occurs at low temperature so that the experimentally observed behaviour is recovered (slower cation diffusion near room temperature).⁷¹ This result is due to the fact that ion/polymer correlations are less dominant at high temperatures, so that diffusion is mostly driven by the size of the ion (reciprocally, diffusion at low temperatures is mostly driven by ion/ion and ion/polymer interactions and is, therefore, less sensitive to the ion sizes). Second, while D_s for Li^+ is nearly independent of c_s , D_s for PF_6^- decreases significantly upon increasing salt concentration (from $1.5 \times 10^{-14} \text{ m}^2/\text{s}$ at 0.32 mol/kg to $0.2 \times 10^{-14} \text{ m}^2/\text{s}$ above 1.3 mol/kg). We note that D_s at low c_s and its decrease could be overestimated by our linear model used to extrapolate the data at high temperatures to near room temperature. However, in any case, this behavior is in agreement with the experimental observations for the reference PEO/LiTFSI-based SPE (e.g. ⁷¹), where the effect of molecular weight and salt concentration on the ionic transport for the PEO/LiTFSI system was investigated by means of NMR. Overall, the data above indicate that – although our PPC/LiPF₆ system behaves qualitatively in a fashion similar to the reference PEO/LiTFSI material – it presents a lower ionic mobility in agreement with previous studies for PPC-based SPE.³⁴

Ionic conductivity. In this section, we address how ion dynamics affects ionic conductivity σ by varying the temperature T and the salt concentration c_s . Following previous work,^{72–74} we performed out-of-equilibrium molecular dynamics simulations under an electric field at

$T = 600, 650, 700$, and 800 K to determine the ionic conductivity σ . In short, an external electric field \mathbf{E} – with $E = |\mathbf{E}|$ ranging from -0.03 to 0.03 V/Å – is applied along the x direction and the resulting ionic current in the same direction $\mathbf{J}_{\text{ion}}(t)$ is monitored along the dipole following the dipole $\mathbf{P}_{\text{ion}}(t)$:

$$\mathbf{P}_{\text{ion}}(t) = \frac{1}{V} \sum_{\text{ion}} q_{\text{ion}} x_{\text{ion}}(t) \quad (5)$$

As shown in Fig. S5 and S6 of the Supporting Information, \mathbf{J}_{ion} data are generally quite accurate with very limited statistical noise. Fig. 6(a) shows the ionic conductivities σ (points) obtained from the slope $\partial J_{\text{ion},x} / \partial E$ as a function of concentration c_s for different temperatures T . As expected, for a given concentration c_s , σ increases upon increasing temperature T . Moreover, for a given temperature T , σ increases with c_s as the density of charge carriers increases – an effect that is enhanced upon increasing the temperature. In order to extrapolate these data to near-room temperature, as illustrated in Fig. S7.(a) of the Supporting Information, we have fitted these ionic conductivity data with the following Arrhenius' law:

$$\sigma_s(c_s, T) = \sigma_s^\infty(c_s) \exp\left(-\frac{E_\sigma(c_s)}{RT}\right). \quad (6)$$

In practice, both the prefactor σ^∞ and activation energy E_σ were determined for each concentration c_s . We also note that the Arrhenius' fits are obtained with very limited statistical noise. Fig. 6(b) shows both the activation energies $E_\sigma(c_s)$ (red circle) and σ^∞ (blue circle) as a function of c_s . E_σ increases by about 1 kcal/mol from 14.4 at $c_s = 0.32$ mol/kg to 15.6 kcal/mol at $c_s = 1.21$ mol/kg. This increase indicates stronger ion-ion interactions and cluster size as c_s increases. The simulated activation energies for conductivity are similar to the value of 15.6 kcal/mol obtained in Ref.⁷⁵ for the semi-crystalline PEO+10 wt.% LiPF₆. For σ^∞ , we also observe a linear increase in c_s as the number of charge carriers. Both parameters were fitted with a linear regression function that represents well the trend observed in the range of c_s considered here.

In order to estimate the impact of ionic correlations on ionic conductivity, we now compare the true ionic conductivity σ to the Nernst-Einstein conductivity σ_{NE} , which can be assessed from the cation and anion diffusivities:^{76,77}

$$\sigma_{\text{NE}} = \frac{e^2}{V k_{\text{B}} T} (N_+ Z_+^2 D_S^+ + N_- Z_-^2 D_S^-), \quad (7)$$

where V is the volume of the system, N_+ and N_- are the numbers of cations and anions, and Z_+e and Z_-e their respective charge. σ_{NE} is considered to be the conductivity of charges that would diffuse without any ionic correlations so that $\sigma_{\text{NE}} \geq \sigma$ at all concentrations c_s . Fig. 6(c) shows σ (solid line) and σ_{NE} (dashed line) as a function of c_s as extrapolated to a temperature of $T = 353$ K using Arrhenius' laws. The points represent the direct prediction for each SPE obtained with Arrhenius' law. Interestingly, an ionic conductivity optimum of $\sim 6.5 \times 10^{-5}$ S/cm is observed for a salt concentration between 1.0 and 1.1 mol/kg [see Fig. S7(b) of the Supporting Information]. Although this conductivity maximum is in the salt concentration range expected experimentally (see for instance⁵³), we note that here that it is a true prediction from our molecular simulation data obtained at high temperature. In particular, for the range of salt concentrations under study, this optimum is not observed in the high-temperature data so that it really corresponds to a physical effect that only occurs at low to moderate temperatures [*e.g.* the decrease of the mobility of the ionic species due to ion/polymer and ion/ion interactions as illustrated in Fig. S8(a) of the Supporting Information]. Furthermore, the conductivity σ at $T = 300$ K is one order of magnitude lower with a maximum of 1.3×10^{-6} S/cm, which is similar to the experimental value reported for PPC-LiBOB SPE.²¹ For σ_{NE} at $T = 353$ K, we also observe an optimum $\sim 1.5 \times 10^{-3}$ S/cm around 0.6 mol/kg. Given these values, a factor of about 20 is observed between the Nernst-Einstein and real conductivities along with a shift in the optimum toward lower salt concentrations. Such differences can be explained by the fact that important ion-ion interactions in SPE (including ion pairing) are not taken into account in the Nernst-Einstein conductivity.⁷⁸ It

was also demonstrated that the gap between both conductivities is enhanced by the viscosity of the system.⁷⁹

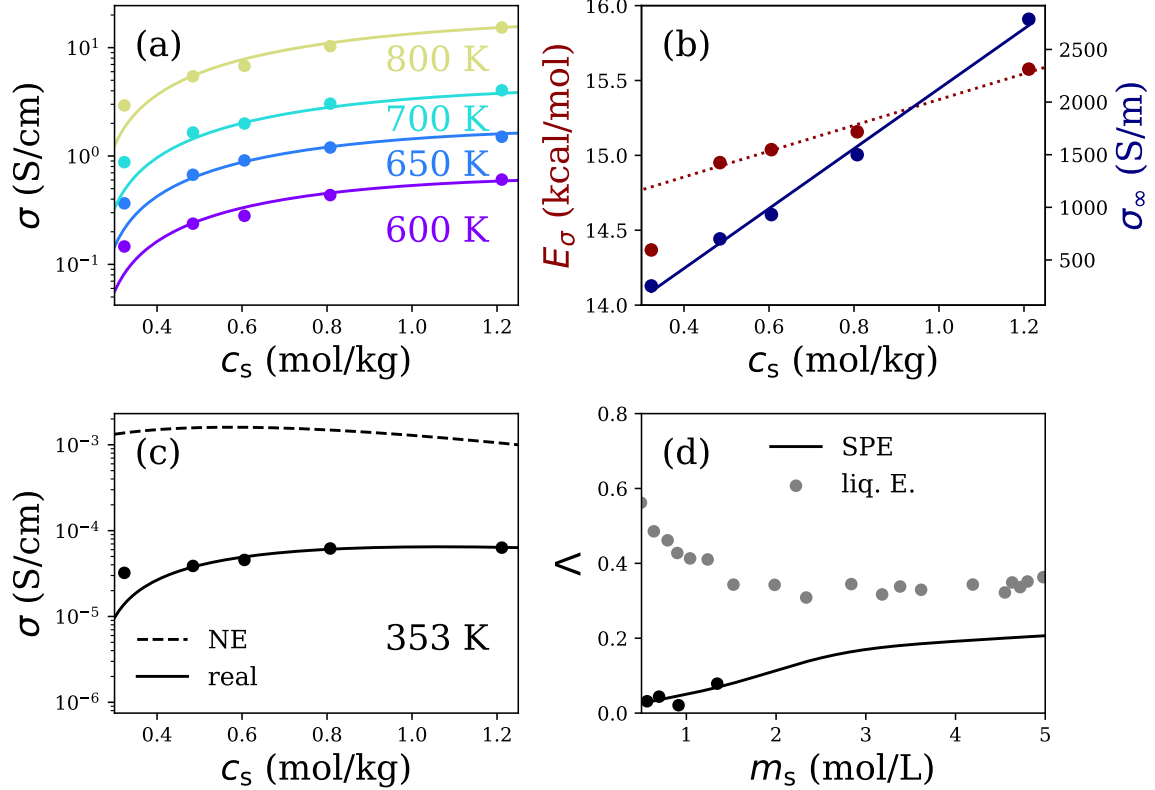


Figure 6: (a) Ionic conductivity σ as a function of the salt concentration c_s for $T = 600$ K, 650 K, 700 K and 800 K. (b) Activation energy E_σ (red) and σ_∞ (blue) for the ionic conductivity σ as a function of c_s . The points corresponds to data while the lines are linear regressions. (c) Real (straight line) and Nernst-Einstein (dashed line) ionic conductivities at $T = 353$ K as a function of c_s predicted from high temperature data using Arrhenius' law (see text). (d) ionicity Λ at 353 K for the SPE (black) and for liquid electrolytes LiBF₄ in ethylene carbonate issued from ref.⁵³

Physico-chemical parameters are important to determine if an electrolyte is a good candidate for electrochemical applications. Among such quantities, the ionicity can be defined as the ratio of the true *versus* the ideal conductivity.

$$\Lambda = \frac{\sigma}{\sigma_{\text{NE}}} \quad (8)$$

Λ quantifies the degree of dynamic ion correlations in the system. Fig. 6(d) shows Λ for our

SPE at $T = 353$ K along with a qualitative sketch illustrating the anticipated trend for liquid carbonate electrolytes. Λ for the other temperatures of our SPE are plotted in Fig. S8(b) of the Supporting Information. As expected, Λ decreases as the temperature decreases at a given concentration c_s due to the stronger ion correlations in the SPE under near room temperature conditions. Interestingly, Λ does not decrease with c_s as commonly observed for electrolytes due to the increase in the ion-ion correlations at large salt concentrations. For all temperatures, Λ increases with c_s which departs from the common picture for electrolyte solutions.⁵³ We note that the increase between 0.5 and 1.21 mol/kg for all temperatures is very small (< 0.1) (such variations are more pronounced for liquid electrolytes^{53,80}). Λ value is less than 0.1 at near-room temperature, therefore suggesting that the Nernst-Einstein relation is not adequate to model the SPE transport properties. Such pronounced correlations are consistent with the structural analysis above, which showed that ions in SPE form a significant number of contact ion pairs and show a clear tendency to cluster even at the lowest concentration.⁸¹ We also note that the ionicity Λ is almost concentration independent in the range of 0.6-1.3 mol/kg for temperatures above $T = 700$ K, while it increases with c_s at higher temperatures. This is due to thermal motion at temperatures large enough such that $k_B T$ is comparable to or larger than the dissociation energy (therefore leading to more decorrelated ion transport). As a result, since the ionicity is defined as a per ion quantity, it becomes concentration independent provided that the ionic conductivity pertains to this decorrelated transport regime.

4. Conclusion

In this work, we investigated by means of Molecular Dynamics simulations the interplay between structure and dynamics in solid polymer electrolytes composed of polypropylene carbonate with different salt concentrations c_s of lithium hexafluorophosphate. Such PPC/LiPF₆-based SPE exhibit strong ion-ion interactions (*i.e.*, ion association) as revealed by the small

fraction of free ions and the large fraction of ions involved in contact ion pairs and ion clusters. The number of free Li^+ cations slightly exceeds that of PF_6^- anions, therefore leading to ionic clusters that tend to be neutral or negatively charged as their size increases (the negative charge of these clusters induces the mobility of Li^+ cation by migration in the opposite direction to the Li^+ concentration gradient induced by electrochemical reactions). This effect is further enhanced by the length of the polymer chain. Such SPE are low dielectric media so that electrostatic interactions are a key parameter to model these systems (as a result of only partial/inefficient coulomb screening). For the short chain polymer ($n = 3$), the simulated $\epsilon \simeq 1.4\epsilon_0$ – which is almost the value for the polymer made up of long chains ($n = 40$). Consequently, the distribution of ions into the three different states – single free ion, CIP and ion cluster at 1.21 mol/kg – follows the same trend for both the short-chain and long-chain polymers with variations attributed to the conformational constraints imposed by the extensive polymer chain length (we observed a somehow larger number of positive clusters of small size for the short chain SPE, Fig. S2).

To assess ion transport at $T = 353$ K, where the relaxation time scale exceeds that accessible in typical molecular dynamics simulations, we employed a scaling based on Arrhenius' law. We found that this method, which reproduces the expected behavior of SPEs at $T = 353$ K, is a powerful tool that can be used for more complex setups (including electrolyte/electrode interfaces). Transport was first analysed by considering ionic self-diffusivities. While increasing the temperature leads to ion diffusion enhancement (especially that of Li^+ cation), the interaction $\text{Li}^+/\text{carbonate}$ weakens with temperature so that it enhances the solvation/desolvation process of Li^+ cations. Also, we observed that D_s becomes concentration independent upon decreasing the temperature. The dynamics of the cations are strongly coupled to that of the segmental motion of the polymer – as evidenced by the amplitudes of the main peak in the radial distribution functions $g_{\text{Li}-\text{O}}(r)$. This marked interplay arises from the strong polymer/cation interactions. Anions, on the other hand, interact only weakly with the polymer matrix, therefore leading to faster diffusion compared to that

of the cations at low c_s . As c_s increases, the decrease in the self-diffusion coefficient of PF_6^- anion is attributed to ion pairing in these low-dielectric media as mentioned above. This interpretation is further supported by the amplitudes of the radial distribution functions $g_{\text{P}-\text{O}}(r)$ and $g_{\text{P}-\text{Li}}(r)$, which confirm that the anion interacts weakly with the polymer but quite strongly with the counterion.

Collective ion transport was also quantified by estimating the ionic conductivity σ . By extrapolating our high temperature data to $T = 353$ K, we found an optimum in the ionic conductivity at about $c_s = 1.1$ mol/kg. This conductivity optimum shifts to higher c_s upon increasing T as illustrated in Fig. S8.(a) of the Supporting Information. The conductivity maximum, which is consistent with experimental data on liquid and polymer electrolytes (e.g. 53,82,83), arises from the trade-off between (1) fast transport/small number of charge carriers at low salt concentrations and (2) hindered transport/large number of charge carriers at high salt concentrations. Upon increasing the salt concentration, the viscosity increases so that it reduces the ion mobility and then σ . Moreover, the dissociation state of the salt decreases upon increasing c_s due to the promotion of large cluster formations which can eventually lead to complete structural arrest.⁸ Finally, the ionicity Λ obtained throughout this study indicates limited transport performance of the investigated SPE. Indeed, $\Lambda < 0.1$ at $T = 353$ K suggests strong ion dynamical correlations and confirms that the Nernst-Einstein relation is not adequate to estimate transport properties. Overall, we find that LiPF_6/PPC SPE exhibit diminished transport properties compared to the reference SPE material made up of LiTFSI/PEO . Different strategies – like the addition of plasticizing agents in the SPE (solvent, ionic liquid),^{17,34} the elaboration of composite solid polymer electrolytes,⁸⁴ or the use of a binary salt mixture⁸⁵ – could prove to be a valid and efficient strategy for the rational design of optimized electrolytes.

Acknowledgement

This work was supported by the Center of Excellence in Multifunctional Architectured Materials – CEMAM (grant ANR-10-LABX-44-01) funded by the "Investments for the Future" Program, and by the French National Research Agency under the France 2030 program (Grant ANR-22-PEBA-0002). The computational work was carried out on the (1) HPC resources at GENCI-IDRIS (Grant 2024-104137) and (2) the GRICAD infrastructure (<https://gricad.univ-grenoble-alpes.fr>) which is supported by the Grenoble research communities.

Supporting Information Available

Radial distribution functions for the Li-F correlations, comparison of cluster distribution for short and long chain polymers, mean squared displacements, ionic current as a function of the electric field, Arrhenius plots for the self diffusion coefficients and ionic conductivity.

References

- (1) Dunn, B.; Kamath, H.; Tarascon, J.-M. Electrical Energy Storage for the Grid: A Battery of Choices. *Science* **2011**, *334*, 928–935.
- (2) Bresser, D.; Hosoi, K.; Howell, D.; Li, H.; Zeisel, H.; Amine, K.; Passerini, S. Perspectives of automotive battery R&D in China, Germany, Japan, and the USA. *J. Power Sources* **2018**, *382*, 176–178.
- (3) Titirici, M. et al. 2024 roadmap for sustainable batteries. *JPhys Energy* **2024**, *6*, 041502.
- (4) Zhou, W.; Wang, S.; Li, Y.; Xin, S.; Manthiram, A.; Goodenough, J. B. Plating a Dendrite-Free Lithium Anode with a Polymer/Ceramic/Polymer Sandwich Electrolyte. *J. Am. Chem. Soc* **2016**, *138*, 9385–9388.

(5) Dong, T.; Xu, G.; Xie, B.; Liu, T.; Gong, T.; Sun, C.; Wang, J.; Zhang, S.; Zhang, X.; Zhang, H.; Huang, L.; Cui, G. An Electrode-Crosstalk-Suppressing Smart Polymer Electrolyte for High Safety Lithium-Ion Batteries. *Adv. Mater.* **2024**, *36*, 2400737.

(6) Ngo, H. P. K.; Shao, Y.; Bertaix, T.; Nguyen, T. K. L.; Solier, J.; Planes, E.; Judeinstein, P.; Alloin, F.; Sanchez, J.-Y.; Iojoiu, C. Single-Ion Conducting Polymer Electrolyte with Excellent Interfacial Stability toward the Lithium Metal. *ACS Appl. Energy Mater.* **2025**, *8*, 2819–2827.

(7) Song, Z.; Chen, F.; Martínez-Ibáñez, M.; Feng, W.; Forsyth, M.; Zhou, Z.; Armand, M.; Zhang, H. A reflection on polymer electrolytes for solid-state lithium metal batteries. *Nat. Commun.* **2023**, *14*.

(8) Li, Z.; Fu, J.; Zhou, X.; Gui, S.; Wei, L.; Yang, H.; Li, H.; Guo, X. Ionic Conduction in Polymer-Based Solid Electrolytes. *Adv. Sci.* **2023**, *10*, 2201718.

(9) Chattopadhyay, J.; Pathak, T. S.; Santos, D. M. F. Applications of Polymer Electrolytes in Lithium-Ion Batteries: A Review. *Polymers* **2023**, *15*.

(10) Xue, Z.; He, D.; Xie, X. Poly(ethylene oxide)-based electrolytes for lithium-ion batteries. *J. Mater. Chem. A* **2015**, *3*, 19218–19253.

(11) Thiam, A.; Martinez-Cisneros, C.; Molméret, Y.; Iojoiu, C.; Sanchez, J.-Y. PEO: An immobile solvent? *Electrochim. Acta* **2019**, *302*, 338–343.

(12) Barbosa, J. C.; Gonçalves, R.; Costa, C. M.; Lanceros-Méndez, S. Toward Sustainable Solid Polymer Electrolytes for Lithium-Ion Batteries. *ACS Omega* **2022**, *7*, 14457–14464.

(13) Song, Z.; Chen, F.; Martínez-Ibáñez, M.; Feng, W.; Forsyth, M.; Zhou, Z.; Armand, M.; Zhang, H. A reflection on polymer electrolytes for solid-state lithium metal batteries. *Nat. Commun.* **2023**, *14*.

(14) Li, H. Solid state battery, what's next? *Next Energy* **2023**, *1*, 100007.

(15) Daems, K.; Yadav, P.; Dermenci, K.; Van Mierlo, J.; Berecibar, M. Advances in inorganic, polymer and composite electrolytes: Mechanisms of Lithium-ion transport and pathways to enhanced performance. *Renew. Sustain. Energy Rev.* **2024**, *191*, 114136.

(16) Cheng, Z.; Liu, T.; Zhao, B.; Shen, F.; Jin, H.; Han, X. Recent advances in organic-inorganic composite solid electrolytes for all-solid-state lithium batteries. *Energy Storage Mater.* **2021**, *34*, 388–416.

(17) Zhang, J.; Zhao, J.; Yue, L.; Wang, Q.; Chai, J.; Liu, Z.; Zhou, X.; Li, H.; Guo, Y.; Cui, G.; Chen, L. Safety-Reinforced Poly(Propylene Carbonate)-Based All-Solid-State Polymer Electrolyte for Ambient-Temperature Solid Polymer Lithium Batteries. *Adv. Energy Mater.* **2015**, *5*, 1501082.

(18) Zhao, J.; Zhang, J.; Hu, P.; Ma, J.; Wang, X.; Yue, L.; Xu, G.; Qin, B.; Liu, Z.; Zhou, X.; Cui, G. A sustainable and rigid-flexible coupling cellulose-supported poly(propylene carbonate) polymer electrolyte towards 5V high voltage lithium batteries. *Electrochim. Acta* **2016**, *188*, 23–30.

(19) Yue, H.; Li, J.; Wang, Q.; Li, C.; Zhang, J.; Li, Q.; Li, X.; Zhang, H.; Yang, S. Sandwich-Like Poly(propylene carbonate)-Based Electrolyte for Ambient-Temperature Solid-State Lithium Ion Batteries. *ACS Sustain. Chem. Eng.* **2018**, *6*, 268–274.

(20) Xiao, S.; Ren, L.; Liu, W.; Zhang, L.; Wang, Q. High-voltage polymer electrolytes: Challenges and progress. *Energy Storage Mater.* **2023**, *63*, 102970.

(21) Sashmitha, K.; Rani, M. U. Physical, mechanical, morphological and electrochemical performance of poly (propylene carbonate) based blend polymer electrolyte. *J. Mater. Sci.: Mater. Electron.* **2023**, *34*.

(22) Foran, G. Y.; St-Antoine, C.; Lepage, D.; Cui, M.; Zheng, R.; Prébé, A.; Goward, G. R.; Dollé, M. Impact of functional groups on lithium salt dispersion and mobility in polymer electrolytes. *J. Appl. Polym. Sci.* **2024**, *141*, e56209.

(23) Zhang, Z.; Ren, Y.; Liang, J.; Xiao, M.; Wang, S.; Huang, S.; Han, D.; Meng, Y. Rationally designed poly(propylene carbonate)-based electrolyte for dendrite-free all solid-state lithium metal batteries. *Energy Storage Mater.* **2024**, *71*, 103667.

(24) Du, L. C.; Meng, Y. Z.; Wang, S. J.; Tjong, S. C. Synthesis and degradation behavior of poly(propylene carbonate) derived from carbon dioxide and propylene oxide. *J. Appl. Polym. Sci.* **2004**, *92*, 1840–1846.

(25) Yu, X.-Y.; Xiao, M.; Wang, S.-J.; Zhao, Q.-Q.; Meng, Y.-Z. Fabrication and characterization of PEO/PPC polymer electrolyte for lithium-ion battery. *J. Appl. Polym. Sci.* **2010**, *115*, 2718–2722.

(26) Zhou, D.; Zhou, R.; Chen, C.; Yee, W.-A.; Kong, J.; Ding, G.; Lu, X. Non-Volatile Polymer Electrolyte Based on Poly(propylene carbonate), Ionic Liquid, and Lithium Perchlorate for Electrochromic Devices. *J. Phys. Chem. B* **2013**, *117*, 7783–7789.

(27) Yang, H.; Wu, N. Ionic conductivity and ion transport mechanisms of solid-state lithium-ion battery electrolytes: A review. *Energy sci. eng.* **2022**, *10*, 1643–1671.

(28) Yu, W.; Deng, N.; Feng, Y.; Feng, X.; Xiang, H.; Gao, L.; Cheng, B.; Kang, W.; Zhang, K. Understanding multi-scale ion-transport in solid-state lithium batteries. *eScience* **2025**, *5*, 100278.

(29) Gudla, H.; Shao, Y.; Phunnarungsi, S.; Brandell, D.; Zhang, C. Importance of the Ion-Pair Lifetime in Polymer Electrolytes. *J. Phys. Chem. Let.* **2021**, *12*, 8460–8464.

(30) Mabuchi, T.; Nakajima, K.; Tokumasu, T. Molecular Dynamics Study of Ion Transport in Polymer Electrolytes of All-Solid-State Li-Ion Batteries. *Micromachines* **2021**, *12*.

(31) Shen, K.-H.; Hall, L. M. Effects of Ion Size and Dielectric Constant on Ion Transport and Transference Number in Polymer Electrolytes. *Macromolecules* **2020**, *53*, 10086–10096.

(32) Shen, K.-H.; Hall, L. M. Ion Conductivity and Correlations in Model Salt-Doped Polymers: Effects of Interaction Strength and Concentration. *Macromolecules* **2020**, *53*, 3655–3668.

(33) Rajahmundry, G. K.; Patra, T. K. Understanding Ion Distribution and Diffusion in Solid Polymer Electrolytes. *Langmuir* **2024**, *40*, 18942–18949.

(34) Gerlitz, A. I.; Diddens, D.; Grünebaum, M.; Heuer, A.; Winter, M.; Wiemhöfer, H.-D. Polypropylene carbonate-based electrolytes as model for a different approach towards improved ion transport properties for novel electrolytes. *Phys. Chem. Chem. Phys.* **2023**, *25*, 4810–4823.

(35) Jorgensen, W. L.; Maxwell, D. S.; Tirado-Rives, J. Development and Testing of the OPLS All-Atom Force Field on Conformational Energetics and Properties of Organic Liquids. *J. Am. Chem. Soc.* **1996**, *118*, 11225–11236.

(36) Silva, L. B.; Freitas, L. C. G. Structural and thermodynamic properties of liquid ethylene carbonate and propylene carbonate by Monte Carlo Simulations. *J. Mol. Struct. THEOCHEM* **2007**, *806*, 23–34.

(37) Canongia Lopes, J. N.; Deschamps, J.; Pádua, A. A. H. Modeling Ionic Liquids Using a Systematic All-Atom Force Field. *J. Phys. Chem. B* **2004**, *108*, 2038–2047.

(38) Canongia Lopes, J. N.; Deschamps, J.; Pádua, A. A. H. Modeling Ionic Liquids Using a Systematic All-Atom Force Field. *J. Phys. Chem. B* **2004**, *108*, 11250–11250.

(39) Costa, L. T.; Sun, B.; Jeschull, F.; Brandell, D. Polymer-ionic liquid ternary systems

for Li-battery electrolytes: Molecular dynamics studies of LiTFSI in a EMIm-TFSI and PEO blend. *J. Chem. Phys.* **2015**, *143*, 024904.

(40) Mogurampelly, S.; Ganesan, V. Structure and mechanisms underlying ion transport in ternary polymer electrolytes containing ionic liquids. *J. Chem. Phys.* **2017**, *146*, 074902.

(41) Eastwood, J.; Hockney, R.; Lawrence, D. P3M3DP—The three-dimensional periodic particle-particle/ particle-mesh program. *Comput. Phys. Commun.* **1980**, *19*, 215–261.

(42) Thompson, A. P.; Aktulga, H. M.; Berger, R.; Bolintineanu, D. S.; Brown, W. M.; Crozier, P. S.; in 't Veld, P. J.; Kohlmeyer, A.; Moore, S. G.; Nguyen, T. D.; Shan, R.; Stevens, M. J.; Tranchida, J.; Trott, C.; Plimpton, S. J. LAMMPS - a flexible simulation tool for particle-based materials modeling at the atomic, meso, and continuum scales. *Comput. Phys. Commun.* **2022**, *271*, 108171.

(43) Brown, W. M.; Wang, P.; Plimpton, S. J.; Tharrington, A. N. Implementing Molecular Dynamics on Hybrid High Performance Computers – Short Range Forces. *Comput. Phys. Commun.* **2011**, *182*, 898–911.

(44) Brown, W. M.; Kohlmeyer, A.; Plimpton, S. J.; Tharrington, A. N. Implementing Molecular Dynamics on Hybrid High Performance Computers – Particle–Particle Particle-Mesh. *Comput. Phys. Commun.* **2012**, *183*, 449–459.

(45) Verlet, L.; Levesque, D. On the Theory of Classical Fluids II. *Physica* **1962**, *28*, 1124–1142.

(46) Verlet, L. Computer "Experiments" on Classical Fluids. I. Thermodynamical Properties of Lennard-Jones Molecules. *Phys. Rev.* **1967**, *159*, 98–103.

(47) Ryckaert, J.-P.; Ciccotti, G.; Berendsen, H. J. Numerical integration of the cartesian

equations of motion of a system with constraints: molecular dynamics of n-alkanes. *J. Comput. Phys.* **1977**, *23*, 327–341.

(48) Evans, D. J.; Holian, B. L. The Nose–Hoover thermostat. *J. Phys. Chem.* **1985**, *83*, 4069–4074.

(49) Wagner, M. H.; Narimissa, E.; Masubuchi, Y. Elongational viscosity of poly(propylene carbonate) melts: tube-based modelling and primitive chain network simulations. *Rheol. Acta* **2023**, *62*, 1–14.

(50) Wang, Y.-Q.; Xu, H.; Cao, B.; Ma, J.; Yu, Z.-W. In Situ Species Analysis of a Lithium-Ion Battery Electrolyte Containing LiTFSI and Propylene Carbonate. *J. Phys. Chem. Lett.* **2024**, *15*, 5047–5055.

(51) Borodin, O.; Smith, G. D.; Jaffe, R. L. Ab initio quantum chemistry and molecular dynamics simulations studies of LiPF₆/poly(ethylene oxide) interactions. *J. Comput. Chem.* **2001**, *22*, 641–654.

(52) Ravikumar, B.; Mynam, M.; Rai, B. Molecular dynamics investigation of electric field altered behavior of lithium ion battery electrolytes. *J. Mol. Liq.* **2020**, *300*, 112252.

(53) Skarmoutsos, I.; Mossa, S. Length scales in electrolytes. *J. Chem. Phys.* **2025**, *163*, 054502.

(54) Skarmoutsos, I.; Ponnuchamy, V.; Vetere, V.; Mossa, S. Li⁺ Solvation in Pure, Binary, and Ternary Mixtures of Organic Carbonate Electrolytes. *J. Phys. Chem. C* **2015**, *119*, 4502–4515.

(55) Ponnuchamy, V.; Mossa, S.; Skarmoutsos, I. Solvent and Salt Effect on Lithium Ion Solvation and Contact Ion Pair Formation in Organic Carbonates: A Quantum Chemical Perspective. *J. Phys. Chem. C* **2018**, *122*, 25930–25939.

(56) Kameda, Y.; Umebayashi, Y.; Takeuchi, M.; Wahab, M. A.; Fukuda, S.; Ishiguro, S.-i.; Sasaki, M.; Amo, Y.; Usuki, T. Solvation Structure of Li⁺ in Concentrated LiPF₆-Propylene Carbonate Solutions. *J. Phys. Chem. B* **2007**, *111*, 6104–6109.

(57) Kameda, Y.; Saito, S.; Umebayashi, Y.; Fujii, K.; Amo, Y.; Usuki, T. Local structure of Li⁺ in concentrated LiPF₆-dimethyl carbonate solutions. *J. Mol. Liq.* **2016**, *217*, 17–22, Special issue in honor of Prof. Arakawa.

(58) Vatin, M.; Duvail, M.; Guilbaud, P.; Dufrêche, J.-F. Thermodynamics of Malonamide Aggregation Deduced from Molecular Dynamics Simulations. *J. Phys. Chem. B* **2021**, *125*, 3409–3418.

(59) Molinari, N.; Mailoa, J. P.; Kozinsky, B. Effect of Salt Concentration on Ion Clustering and Transport in Polymer Solid Electrolytes: A Molecular Dynamics Study of PEO–LiTFSI. *Chem. Mat.* **2018**, *30*, 6298–6306.

(60) Neumann, M. Dipole moment fluctuation formulas in computer simulations of polar systems. *Mol. Phys.* **1983**, *50*, 841–858.

(61) Rieger, B.; Kunkel, A.; Coates, G.; Reichardt, R.; Dinjus, E.; Zevaco, T. *Synthetic Biodegradable Polymers*; Advances in Polymer Science; Springer, 2012; Vol. 245; pp 1–364.

(62) Rullyani, C.; Sung, C.-F.; Lin, H.-C.; Chu, C.-W. Flexible Organic Thin Film Transistors Incorporating a Biodegradable CO₂-Based Polymer as the Substrate and Dielectric Material. *Sci. Rep.* **2018**, *8*.

(63) Payne, R.; Theodorou, I. E. Dielectric properties and relaxation in ethylene carbonate and propylene carbonate. *J. Phys. Chem.* **1972**, *76*, 2892–2900.

(64) Hall, D. S.; Self, J.; Dahn, J. R. Dielectric Constants for Quantum Chemistry and Li-

Ion Batteries: Solvent Blends of Ethylene Carbonate and Ethyl Methyl Carbonate. *J. Phys. Chem. C* **2015**, *119*, 22322–22330.

(65) Zhang, Q.-K.; Zhang, X.-Q.; Yuan, H.; Huang, J.-Q. Thermally Stable and Non-flammable Electrolytes for Lithium Metal Batteries: Progress and Perspectives. *Small Science* **2021**, *1*, 2100058.

(66) Yao, N.; Chen, X.; Shen, X.; Zhang, R.; Fu, Z.-H.; Ma, X.-X.; Zhang, X.-Q.; Li, B.-Q.; Zhang, Q. An Atomic Insight into the Chemical Origin and Variation of the Dielectric Constant in Liquid Electrolytes. *Angew. Chem., Int. Ed. Engl.* **2021**, *60*, 21473–21478.

(67) Pranami, G.; Lamm, M. H. Estimating Error in Diffusion Coefficients Derived from Molecular Dynamics Simulations. *J. Chem. Theory Comput.* **2015**, *11*, 4586–4592.

(68) Kellouai, W.; Judeinstein, P.; Plazanet, M.; Zanotti, J.-M.; Berrod, Q.; Drobek, M.; Julbe, A.; Coasne, B. Free volume theory of self-diffusion in zeolites: Molecular simulation and experiment. *Micropor. Mesopor. Mat.* **2025**, *381*, 113305.

(69) Diederichsen, K. M.; Buss, H. G.; McCloskey, B. D. The Compensation Effect in the Vogel–Tamman–Fulcher (VTF) Equation for Polymer-Based Electrolytes. *Macromolecules* **2017**, *50*, 3831–3840.

(70) Aziz, S. B.; Woo, T. J.; Kadir, M.; Ahmed, H. M. A conceptual review on polymer electrolytes and ion transport models. *J. Sci.: Adv. Mater. Devices* **2018**, *3*, 1–17.

(71) Timachova, K.; Watanabe, H.; Balsara, N. P. Effect of Molecular Weight and Salt Concentration on Ion Transport and the Transference Number in Polymer Electrolytes. *Macromolecules* **2015**, *48*, 7882–7888.

(72) Hartkamp, R.; Coasne, B. Structure and transport of aqueous electrolytes: From simple halides to radionuclide ions. *J. Chem. Phys.* **2014**, *141*, 124508.

(73) Cazade, P.-A.; Hartkamp, R.; Coasne, B. Structure and Dynamics of an Electrolyte Confined in Charged Nanopores. *J. Phys. Chem. C* **2014**, *118*, 5061–5072.

(74) Cox, S. J.; Sprik, M. Finite field formalism for bulk electrolyte solutions. *Journal Chem. Phys.* **2019**, *151*, 064506.

(75) Chaurasia, S. K.; Saroj, A. L.; Shalu; Singh, V. K.; Tripathi, A. K.; Gupta, A. K.; Verma, Y. L.; Singh, R. K. Studies on structural, thermal and AC conductivity scaling of PEO-LiPF₆ polymer electrolyte with added ionic liquid [BMIMPF₆]. *AIP Advances* **2015**, *5*, 077178.

(76) Maginn, E. J.; Messerly, R. A.; Carlson, D. J.; Roe, D. R.; Elliot, J. R. Best Practices for Computing Transport Properties 1. Self-Diffusivity and Viscosity from Equilibrium Molecular Dynamics [Article v1.0]. *Living J. Comput. Mol. Sci.* **2018**, *1*, 6324.

(77) Verma, A. K.; Thorat, A. S.; Shah, J. K. Estimating ionic conductivity of ionic liquids: Nernst–Einstein and Einstein formalisms. *J. Ionic Liquids* **2024**, *4*, 100089.

(78) Pang, M.-C.; Marinescu, M.; Wang, H.; Offer, G. Mechanical behaviour of inorganic solid-state batteries: can we model the ionic mobility in the electrolyte with Nernst–Einstein’s relation? *Phys. Chem. Chem. Phys.* **2021**, *23*, 27159–27170.

(79) Shao, Y.; Shigenobu, K.; Watanabe, M.; Zhang, C. Role of Viscosity in Deviations from the Nernst–Einstein Relation. *J. Phys. Chem. B* **2020**, *124*, 4774–4780, PMID: 32412758.

(80) Teherpuria, H.; Paul Chowdhury, S. S.; Kannam, S. K.; Jaiswal, P. K.; Mogurampelly, S. Salt Effects on Ionic Conductivity Mechanisms in Ethylene Carbonate Electrolytes: Interplay of Viscosity and Ion–Ion Relaxations. *ACS Macro Lett.* **2025**, *14*, 802–807, PMID: 40418196.

(81) France-Lanord, A.; Grossman, J. C. Correlations from Ion Pairing and the Nernst-Einstein Equation. *Phys. Rev. Lett.* **2019**, *122*, 136001.

(82) Logan, E. R.; Tonita, E. M.; Gering, K. L.; Li, J.; Ma, X.; Beaulieu, L. Y.; Dahn, J. R. A Study of the Physical Properties of Li-Ion Battery Electrolytes Containing Esters. *J. Electrochem. Soc.* **2018**, *165*, A21–A30.

(83) Bolloli, M.; Alloin, F.; Kalhoff, J.; Bresser, D.; Passerini, S.; Judeinstein, P.; Leprêtre, J.-C.; Sanchez, J.-Y. Effect of carbonates fluorination on the properties of LiTFSI-based electrolytes for Li-ion batteries. *Electrochim. Acta* **2015**, *161*, 159–170.

(84) Zhu, L.; Li, J.; Jia, Y.; Zhu, P.; Jing, M.; Yao, S.; Shen, X.; Li, S.; Tu, F. Toward high performance solid-state lithium-ion battery with a promising PEO/PPC blend solid polymer electrolyte. *Int. J. Energy Res.* **2020**, *44*, 10168–10178.

(85) Li, H.; Du, Y.; Wu, X.; Xie, J.; Lian, F. Developing “Polymer-in-Salt” High Voltage Electrolyte Based on Composite Lithium Salts for Solid-State Li Metal Batteries. *Adv. Funct. Mater.* **2021**, *31*, 2103049.